Rare Met. (2022) 41(2):396–405
https://doi.org/10.1007/s12598-021-01784-3

RARE METALS

ORIGINAL ARTICLE

Hierarchical porous NiO as a noble-metal-free cocatalyst for enhanced photocatalytic H_2 production of nitrogen-deficient g-C_3N_4

Yu-Wei Liao, Jing Yang, Guo-Hong Wang*, Juan Wang, Kai Wang, Su-Ding Yan

Received: 30 December 2020 / Revised: 7 March 2021 / Accepted: 31 March 2021 / Published online: 17 July 2021

Abstract Graphitic carbon nitride with nitrogen vacancies (NV-g-C_3N_4) as a photocatalyst has been studied in solar-driven energy conversion. However, expensive and rare noble metal co-catalysts such as Pt or Pd are required in the photocatalytic H_2 evolution. Consequently, the exploration of low-cost and high-performance co-catalysts to replace expensive and rare noble metals has received more and more attention. Herein, a novel hierarchical porous NiO anchored on NV-g-C_3N_4 is successfully fabricated. The NV-g-C_3N_4/NiO photocatalysts exhibited outstanding H_2 evolution rate under visible light irradiation in absence of noble metal co-catalysts. The optimized NV-g-C_3N_4/NiO (the mass ratio of NiO is $\sim$ 1.7%) achieved a maximum H_2 evolution rate of 170.60 μmol·g^{-1}·h^{-1}, exhibiting $\sim$ 8.3-fold enhancement as compared to that of NV-g-C_3N_4. NiO as co-catalyst provided more active sites for photocatalytic H_2 evolution. Moreover, on the interface of NV-g-C_3N_4/NiO, an interface electric field is formed between NiO and host nitrogen-vacated g-C_3N_4, facilitating the transfer of the photogenerated electrons from NV-g-C_3N_4 to NiO co-catalyst, resulting in significantly promoted migration and separation efficiency of the photogenerated charge carriers.

Keywords Graphitic carbon nitride; Hierarchical porous; NiO; Photocatalysis; H_2 evolution

Y.-W. Liao, J. Yang, G.-H. Wang*, J. Wang, K. Wang, S.-D. Yan
College of Chemistry and Chemical Engineering, Hubei Normal University, Huangshi 435002, China
e-mail: wanggh2003@163.com

Y.-W. Liao, J. Yang, G.-H. Wang, J. Wang, K. Wang
Hubei Key Laboratory of Pollutant Analysis and Reuse Technology, Hubei Normal University, Huangshi 435002, China

1 Introduction

With the aggravation of environmental contamination and the increment of energy consumption, H_2 evolution is one of the promising solutions to alleviate the energy crisis and gain environmental-friendly resources [1–3]. In recent years, photocatalysis is considered as a potential way to reduce water into H_2 by using semiconductor photocatalysts [4–7]. Graphitic carbon nitride (g-C_3N_4), as a polymetric photocatalyst, firstly reported by Wang et al. has been proverbially investigated due to its easy availability, non-toxicity and durable chemical stability [8]. Among the modification methods of g-C_3N_4, the introduction of nitrogen defects into the g-C_3N_4 framework significantly enhanced the photocatalytic activity of g-C_3N_4 under visible light excitation on account of the narrower band gaps obtained. Moreover, nitrogen-vacated g-C_3N_4 (NV-g-C_3N_4) was approved to have greater photocatalytic performance because of its attractive electronic structure, and the preparation method was the same as preceding literatures [9–11].

Even though the introduction of nitrogen defects into the g-C_3N_4 framework accelerates the photoinduced carriers' separation, the high recombination rate of photogenerated charge carriers and the poor quantum efficiency still need to be solved in further research. Usually, sacrificial reagents and co-catalysts are necessary to promote charge separation during the process of solar-driven water splitting. It is generally to load the noble metal co-catalysts, such as Pt nanoparticles, on photocatalysts surface to efficiently enhance charge transfer and realize photocatalytic water splitting [12, 13]. However, from the point of economic perspective, noble metal co-catalysts are too expensive and will be greatly limited in practical applications. Thus, it is of great importance to find an abundant,

low-cost co-catalyst in the photocatalytic hydrogen evolution reaction of g-C_3N_4-based photocatalyst.

The transition metal-based oxides, such as Fe, Co, Ni, Cu and Zn which are abundant and eco-friendly compounds, have been intensively considered as effective co-catalysts for above purpose [14–18]. Nickel oxide (NiO), as a transition metal monoxide, exhibits excellent electrochemical capacitance, oxygen sensitivity and thermal stability in photocatalysis application [19]. Recently, foam-like NiO with hierarchical macroporous/microspheric structure has been synthesized and acted as a novel material in photoredox catalysis [20]. Generally speaking, introducing NiO could efficiently separate photoinduced electrons, further be used as a highly efficient co-catalyst to promote hydrogen evolution reaction. To the best of our knowledge, the NV-g-C_3N_4/NiO composite photocatalysts have rarely been reported so far.

Herein, we firstly design a hierarchical porous NiO co-catalyst decorated NV-g-C_3N_4, which exhibits excellent hydrogen generation performance under visible light irradiation. It is found that ~ 1.7 wt% NiO modified NV-g-C_3N_4 shows the optimal hydrogen evolution activity with the rate of 170.60 $\mu mol \cdot g^{-1} \cdot h^{-1}$ under visible light, which is ~ 8.3 times higher than that of NV-g-C_3N_4.

2 Experimental

2.1 Materials

Dicyandiamide ($C_2H_4N_4$, Sinopharm Chemical Reagent Co., Ltd, ≥ 98%), peanut oil (ordinary supermarket), dimethylglyoxime ($C_4H_8N_2O_2$, Tianjin Kemiou Chemical Testing Co., Ltd, ≥ 98%), nickel acetate tetrahydrate ($Ni(CH_3COO)_2 \cdot 4H_2O$, Guangdong Guanghua Sci-Tech Co., Ltd, ≥ 98.5%) and absolute ethanol (CH_3CH_2OH, Shanghai Wokai Biotechnology Co., Ltd, ≥ 99.5%) were used as received.

2.2 Preparation of hierarchical porous NiO

Hierarchical porous NiO was prepared based on the previous literature [21]. In detail, firstly, 1.25 g $Ni(CH_3COO)_2 \cdot 4H_2O$ was dissolved in 100 ml deionized water and 0.58 g dimethylglyoxime was dissolved in 100 ml absolute ethanol. Secondly, the above two solutions were mixed and then stirred for 2 h. Subsequently, the suspension was filtrated and washed using deionized water and anhydrous ethanol several times to collect the red precipitates. Finally, the red precipitate was dried in vacuum and then calcined in a muffle furnace at 600 °C for 5 h to obtain the hierarchical porous NiO powder.

2.3 Preparation of the NV-g-C_3N_4 photocatalysts

NV-g-C_3N_4 was fabricated via a combined hydrothermal-calcination strategy according to our previous work [22].

2.4 Preparation of NiO decorated NV-g-C_3N_4 photocatalysts

The synthesis illustration of the NiO decorated NV-g-C_3N_4 photocatalysts (named as CNN*x*) is shown in Fig. 1. The CNN*x* samples with different NiO contents were prepared by solvothermal method, where $x = 1$, 2, 3 and 4 correspond to NiO mass of 0.01, 0.02, 0.03 and 0.04 g, respectively. In detail, for CNN3 sample, the previous as-prepared NiO (0.03 g) was dispersed in 2 g precursor of NV-g-C_3N_4 (H-g-C_3N_4) by stirring for 1 h and drying at 60 °C. Then, the powder was calcined in muffle furnace at 550 °C for 6 h to obtain CNN3 sample.

2.5 Sample characterization

X-ray diffractometer (XRD, Bruker AXS, Germany) and Fourier transform infrared spectra (FTIR, Nicolet iS5) were applied to detect structure of the as-prepared CNN*x* samples. Scanning electron microscopy (SEM, ZEISS G300, Germany) and transmission electron microscopy (TEM, Tecnai G20, USA) were used to characterize microstructure and morphology of the samples. The pore volume and average pore size were evaluated using a N_2 adsorption–desorption apparatus (ASAP 2020 HD 88, Micromeritics, USA). Ultraviolet–visible (UV–Vis) spectrophotometer (UV-2450, Shimadzu, Japan) was used to analyze UV–Vis diffuse reflectance spectra (DRS) of the samples. X-ray photoelectron spectroscopy (XPS, K-Alpha, Thermo Scientific) was used to evaluate the bonding status of the as-prepared samples with an Al-Kα X-ray source. Photoluminescence (PL, LS55, Perkinelmer, USA) spectra were recorded under 370-nm excitation wavelength. Fluorescence lifetime spectrophotometer (FLSP920, Edinburgh, UK) was used to obtain time-resolved transient PL decay curves.

2.6 Photocatalytic H_2 evolution

Photocatalytic hydrogen production test was carried out with a closed glass system under 420-nm (3 W) LED light illumination. The produced gases were analyzed by gas chromatograph (SP-7820, TCD, China). For each experiment, 20 mg photocatalyst powder was dispersed in the aqueous solution containing 10 ml sacrificial reagent triethanolamine and 90 ml H_2O in a 100 ml reactor [23].

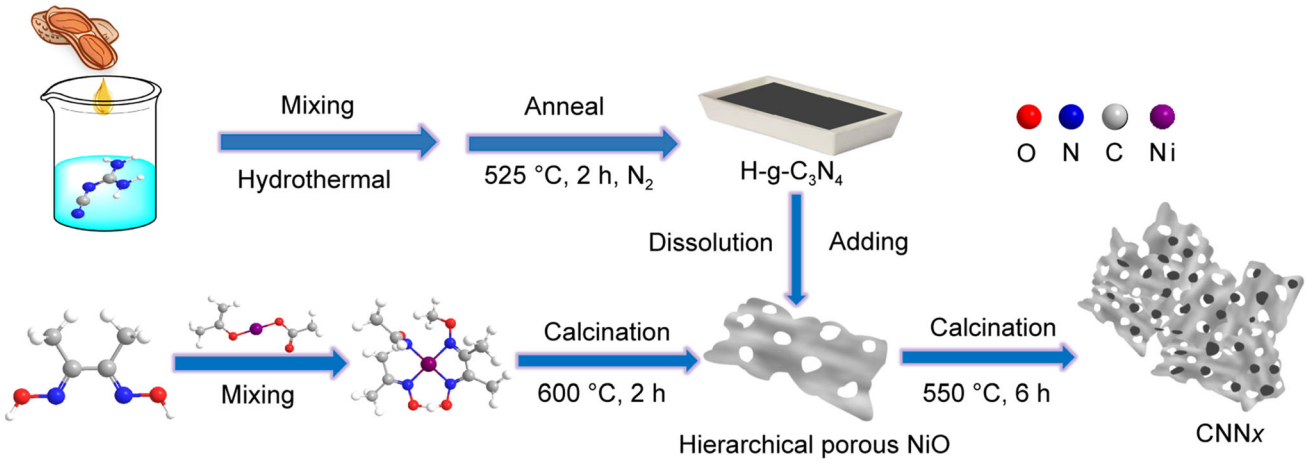

Fig. 1 Synthesis illustration of CNN*x* photocatalysts

2.7 Photoelectrochemical measurements

Photocurrent and impedance characterizations were performed to investigate the photoelectrochemical properties of the as-prepared photocatalysts. In detail, 10 mg as-prepared sample was dispersed in 2.5 ml absolute ethanol to form a homogeneous suspension, and then 0.5 ml suspension was mixed with 0.5 ml nafion solution. After that, the mixture was then spin-coated onto the ITO glass and dried [24]. The photocurrent and impedance measurements were carried out on an electrochemical workstation using a three-electrode system. The above coated ITO glass with as-obtained samples, Pt plate and Ag/AgCl were applied as working electrode, counter electrode and reference electrode, respectively. Moreover, 0.5 mol·L^{-1} Na_2SO_4 and 3 W 420 nm LED lamp were used as electrolyte solution and light source, respectively [25].

2.8 Density functional theory (DFT)

DFT calculations were conducted by Materials Studio. The exchange–correlation energy of generalized gradient approximation (GGA) was adopted in the framework of Perdew-Burke-Ernzerhof (PBE) parametrization. The energy cutoff was set as 400 eV. The *k*-point was chosen as 3 × 3 × 3 and the vacuum spaces were 2 nm. During the geometry optimization, the atomic forces were 0.5 eV·nm^{-1} and ionic convergence criterions were 2 × 10^{-5} eV. The work function is defined by $\varphi = E_{\text{vacuum}}–E_{\text{Fermi}}$, where E_{vacuum} and E_{Fermi} are the electrostatic potentials of the vacuum and Fermi level, respectively [26]. In the geometric structures of NiO (200) and nitrogen-vacated g-C_3N_4, the light blue, red, gray and blue spheres stand for O, Ni, C and N atoms, respectively.

3 Results and discussion

3.1 Physical–chemical characteristics

The morphologies and microstructures of pure NiO and CNN3 were characterized by SEM, TEM and high-resolution transmission electron microscopy (HRTEM). SEM image of the pure NiO in Fig. 2a shows a hierarchical porous structure. As shown in Fig. 2b, as a reference of CNN3, it is interesting to note that some nanosheets are filled into the macropores and covered the walls of NiO skeleton, and the nanosheets might belong to NV-g-C_3N_4. Moreover, TEM and HRTEM were further characterized to investigate the morphology of CNN3 hybrid (Fig. 2c–e). TEM image confirms that there is an intimately contact between NiO and NV-g-C_3N_4, which improves the transfer of photogenerated electron. As seen from HRTEM image (Fig. 2d, e), CNN3 sample exhibits a high crystallinity of NiO, and the lattice fringes of ~ 0.21 and ~ 0.24 nm, corresponding to the (200) and (111) plane of NiO, respectively [27]. As can be seen from Fig. 2f, CNN3 exhibits bimodal pore size distribution located at 3–4 and 40–60 nm, respectively. This result indicates that the modified composite samples exhibit porous structure. In addition, the pore volume and average pore size of CNN3 are 0.26 cm^3·g^{-1} and 26.1 nm, respectively.

Figure 3a displays XRD patterns of NiO, NV-g-C_3N_4 and CNN*x*. For pristine NiO sample, indexed to JCPDS No. 22-1189, the diffraction peaks at 37.2°, 43.2°, 63.1°, 75.5° and 79.3° match well with (111), (200), (220), (311) and (222) crystal planes of NiO, respectively [20, 21]. With further observation from Fig. 3a, the diffraction peak at ~ 43° of obtained NiO corresponding to the (200) plane is observed in CNN4. With the mass of NiO in CNN*x* increasing, the peak intensities of NiO monotonously

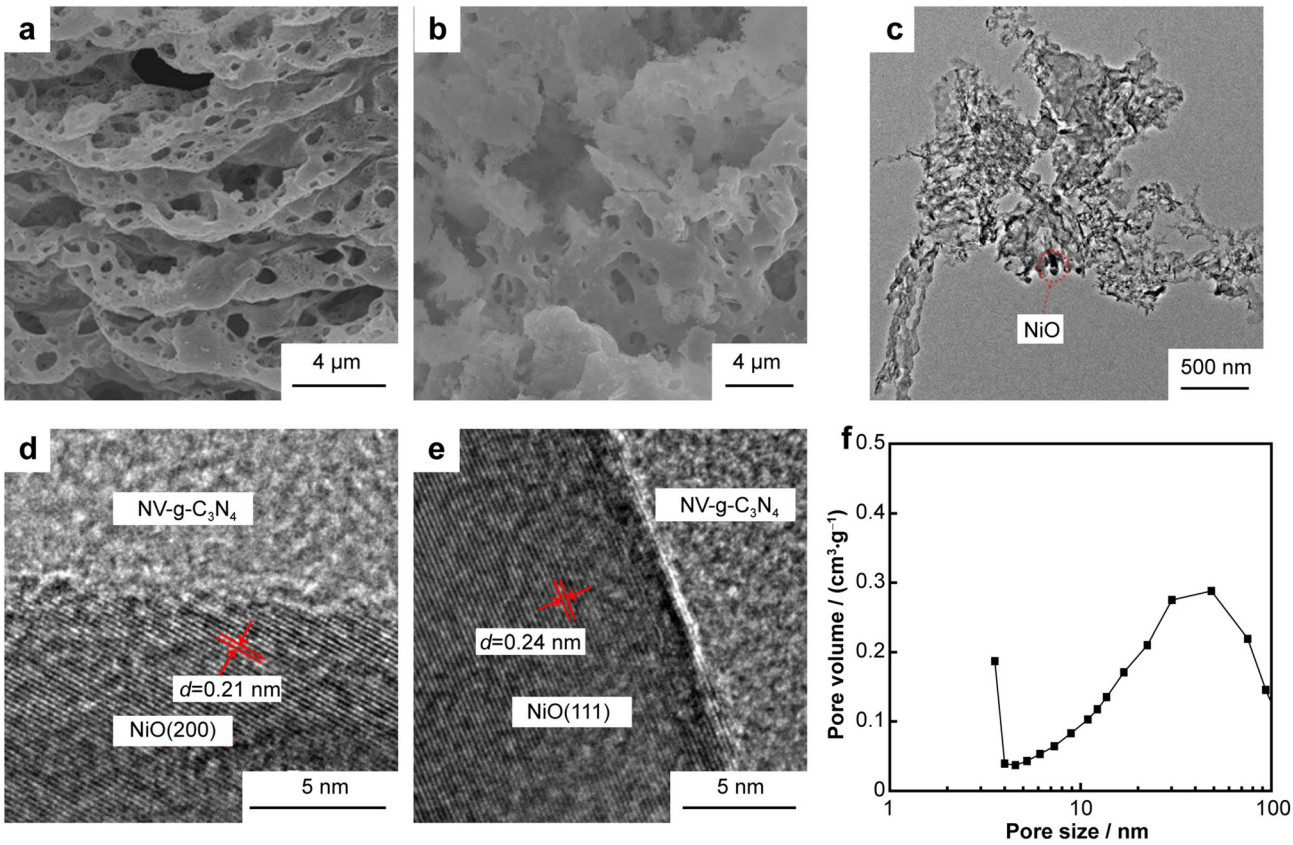

Fig. 2 SEM images of pure **a** NiO and **b** CNN3; **c** TEM, **d-e** HRTEM images and **f** pore size distribution curve of CNN3

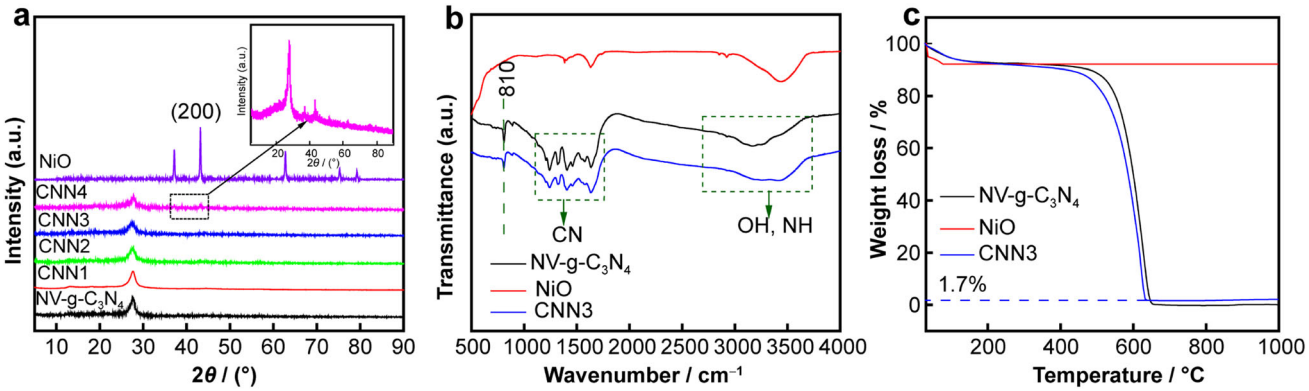

Fig. 3 **a** XRD patterns of pure NiO, NV-g-C_3N_4 and CNN*x*; **b** FTIR spectra and **c** TG curves of pure NiO, NV-g-C_3N_4 and CNN3

increase. In contrast, the peak intensities of NV-g-C_3N_4 gradually decrease.

The functional groups of NiO, NV-g-C_3N_4 and CNN3 were measured by FTIR (Fig. 3b). For the NV-g-C_3N_4 sample, there are several major bands presented at 1150–1700 cm^{-1}, attributing to the C-N heterocycles stretching modes [28]. Meanwhile, the characteristic peak at 810 cm^{-1} corresponded to the triazine units, and the broad peaks at 3100–3400 cm^{-1} were ascribed to N–H and O–H stretching vibration modes [29–31]. Interestingly, FTIR spectrum of CNN3 exhibits the similar peaks with NV-g-C_3N_4, revealing that the structure of CNN3 has not obvious change after loading of NiO.

Figure 3c shows thermo gravimetric (TG) images of NiO, NV-g-C_3N_4 and CNN3 under the atmosphere of O_2. For the pure NiO sample, the weight is hardly lost, indicating the stability of NiO. As for NV-g-C_3N_4, the curve shows two weight lost at around 25–200 and 400–600 °C, ascribing to the loss of absorbed water and the combustion of NV-g-C_3N_4, respectively. Moreover, the sample of

CNN3 also has two weight lost at the same regions as NV-g-C_3N_4, the remaining part of the curve is attributed to the stable NiO. Therefore, the mass ratio of NiO for CNN3 is about 1.7 wt% actually [32].

Meanwhile, the chemical structure and bonding state of the samples were further investigated by XPS analysis, as shown in Fig. 4. In detail, Fig. 4 displays the high-resolution spectra of C 1s, N 1s, O 1s and Ni 2p of CNN3, in good accordance with the composition of CNN3 [33]. Figure 4a gives the high-resolution C 1s XPS results of the CNN3. For CNN3 sample, the curve of C 1s can be deconvoluted into three peaks located at 284.6, 286.2 and 288.1 eV, which are assigned to the C–C bond, C=N bond and N–C=N bond, respectively [34, 35]. The high-resolution XPS spectrum of N 1s is also examined and the results are shown in Fig. 4b. The observed peaks at 398.4, 399.2 and 400.9 eV can be assigned to the C–N=C, N–C_3 and C–N–H, respectively [36]. Moreover, the high-resolution XPS result of O 1s is detected and plotted in Fig. 4c. For CNN3 sample, the O 1s peak exhibits binding energies of 527.3 and 531.9 eV, which are assigned to Ni–O and O–H bonds, respectively [37, 38]. Figure 4d presents the Ni 2p high-resolution spectra of the CNN3 sample, and the two peaks shown at 871.9 and 854.5 eV match with the Ni $2p_{3/2}$ and Ni $2p_{1/2}$ resulted from NiO moiety, respectively, which indicates $a + 2$ valence oxidation state of Ni in NiO [39].

3.2 Photoelectrochemical properties

Figure 5a shows UV–Vis DRS of NV-g-C_3N_4, NiO and CNN3. As can be seen, for the pure NiO sample, effective absorption occurs only in UV region with $\lambda < 380$ nm, while the effective absorption of NV-g-C_3N_4 sample is observed in the visible light [40]. Interestingly, after coupling with NiO, the CNN3 sample also exhibits a similar photo-absorption property with NV-g-C_3N_4. That may be ascribed to the smaller content of NiO (ca. 1.7%) in the CNN3 sample. By plotting the $(Ahv)^2$ versus hv, the E_g of

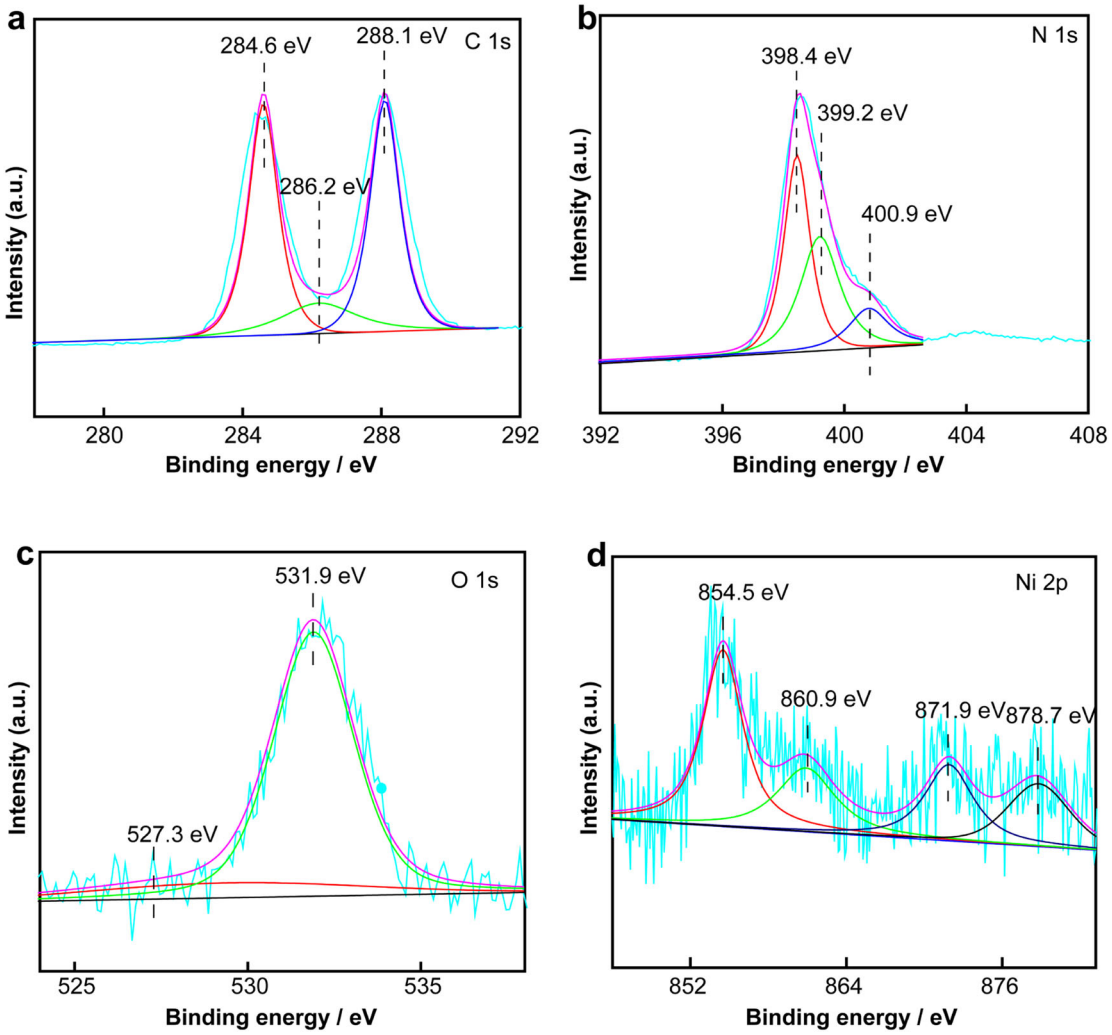

Fig. 4 **a** C 1s, **b** N 1s, **c** O 1s and **d** Ni 2p high-resolution XPS results of CNN3 sample

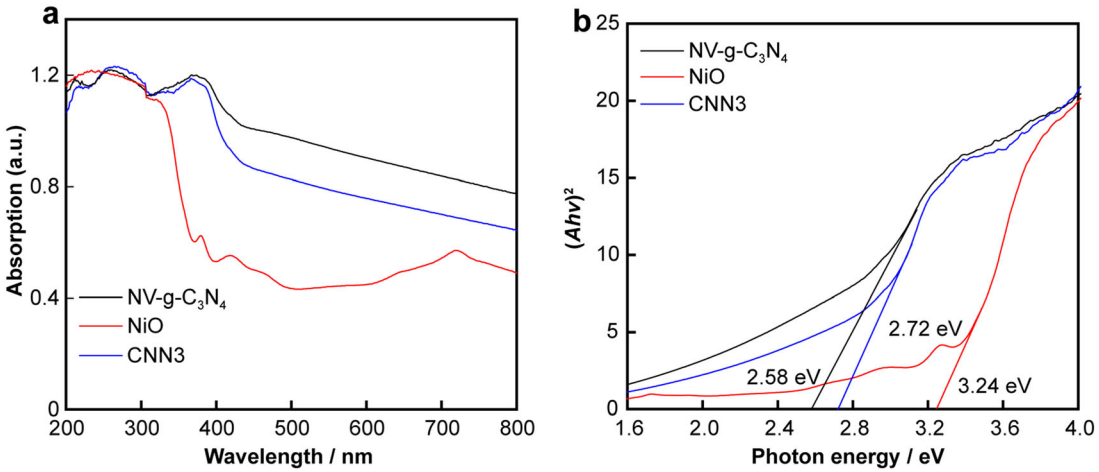

Fig. 5 **a** UV–Vis spectra and **b** plots of $(Ahv)^2$ versus photon energy of pure NiO, NV-g-C_3N_4 and CNN3

the NiO, NV-g-C_3N_4 and CNN3 samples can be estimated from the intercept by linearly fitting the curve, and the results are revealed in Fig. 5b, where h, v and E_g represent the Planck constant, light frequency and band gap energy, respectively [41]. As shown, the fitted E_g values of NV-g-C_3N_4, NiO and CNN3 are 2.58, 3.24 and 2.72 eV, respectively, which match well with their corresponding photo-absorption characteristics [22].

To further explore the separation rate of the photogenerated electrons and holes, the results of photoluminescence analysis are shown in Fig. 6a. In the spectrum of NV-g-C_3N_4, an intensive emission peak at $\sim$ 450 nm is observed, implying the faster recombination of the photoexcited e^-–h^+ pairs for NV-g-C_3N_4 [42]. After introducing NiO, the CNNx composites exhibit the obviously weaker emission peaks at $\sim$ 450 nm, suggesting the efficient separation of photoinduced e^-–h^+ pairs. Noticeably, the CNN3 composite possesses the lowest PL intensity among all the composites, indicating the fastest separation rate of photo-induced carriers in CNN3 [43]. The time-resolved PL measurements were used to further investigate the lifetime of charge carriers for NV-g-C_3N_4 and CNN3 samples, and the curves are shown in Fig. 6b. Obviously, the average fluorescence lifetime of CNN3 (4.640 ns) is longer than that of NV-g-C_3N_4 (4.126 ns), further confirming that CNN3 sample has more efficient carrier separation rate than NV-g-C_3N_4.

Figure 7a shows photocurrent density curves of NV-g-C_3N_4, NiO and CNN3 for photoanode chopping in 0.5 mol·L^{-1} Na_2SO_4 electrolyte under 3 W 420-nm LED light irradiation. Notably, the photocurrent density of NiO is hardly observed because of the relatively large band gap of $\sim$ 3.24 eV (Fig. 5b) [44]. Interestingly, as can be seen in Fig. 7a, CNN3 sample exhibits higher photocurrent density in on and off transitions than pure NiO and NV-g-C_3N_4 samples, meaning that there is a large quantity of photogenerated e^-–h^+ pairs in the system, which is critical for photocatalytic reaction [45]. Furthermore, Fig. 7b

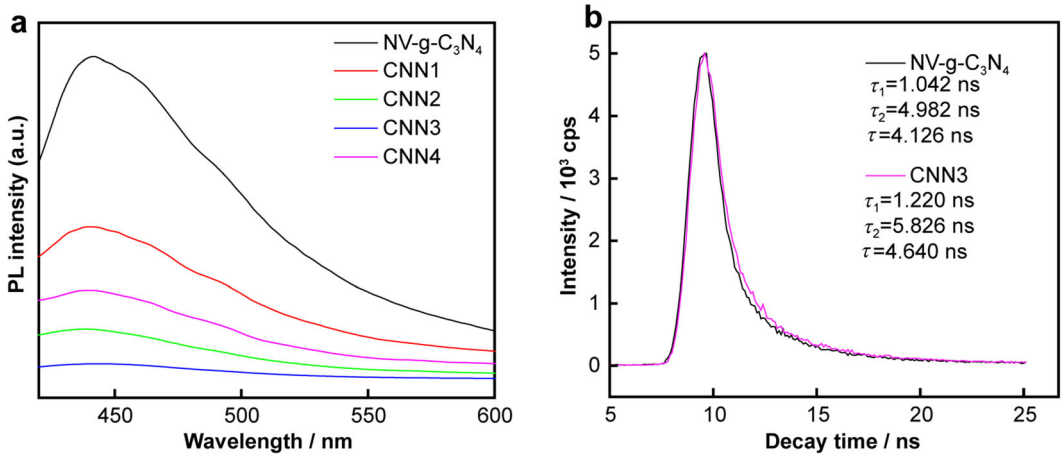

Fig. 6 **a** PL spectra of NV-g-C_3N_4 and CNNx; **b** transient fluorescence spectra of NV-g-C_3N_4 and CNN3

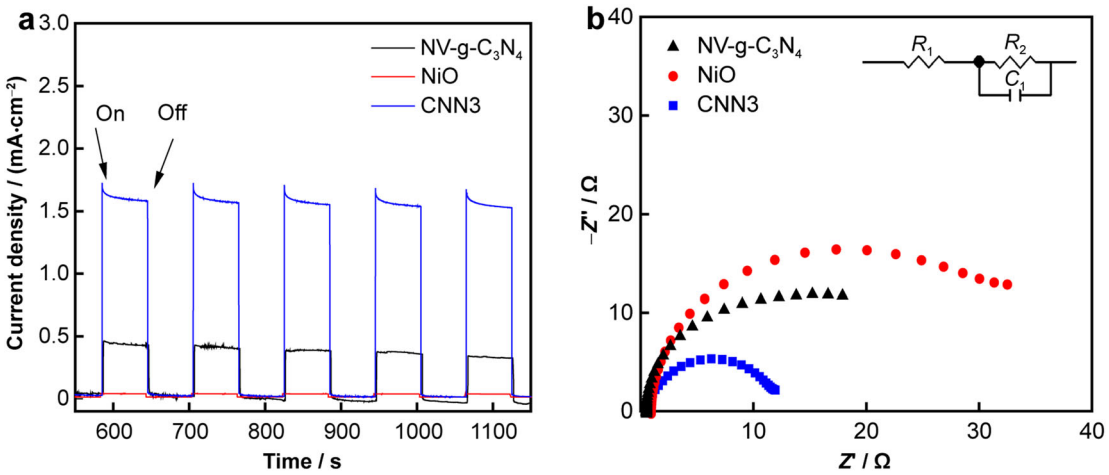

Fig. 7 **a** Transient photocurrent responses and **b** EIS of NiO, NV-g-C_3N_4 and CNN3

presents electrochemical impedance spectroscopy (EIS) results of the as-prepared samples, where Z' and $-Z''$ are the real part and the imaginary part of the impedance, respectively. Obviously, CNN3 sample presents smaller Nyquist arc radius than the singular NiO and NV-g-C_3N_4 samples. It is well known that smaller Nyquist arc radius corresponds to lower charge transfer resistance [46]. The corresponding Nyquist analog equivalent circuit is also given in the inset in Fig. 7b, where R_1, R_2 and C_1 represent the charge-transfer resistance of the electrolyte solution (0.5 mol·L^{-1} Na_2SO_4), working electrode and the constant phase element, respectively [22].

3.3 Photocatalytic hydrogen evolution

To investigate the photocatalytic performance of H_2 production, the as-prepared samples were exposed to visible-light (LED, 420 nm) irradiation. As shown in Fig. 8, the NV-g-C_3N_4 sample has the lowest H_2 production rate of 20.65 μmol·g^{-1}·h^{-1}. That is attributed to the fast recombination of the photoinduced carriers. Surprisingly, after introducing a lower NiO content, the photocatalytic activity of the CNN1 sample (44.15 μmol·g^{-1}·h^{-1}) is obviously enhanced. Further observation indicates that the photocatalytic activity of the NV-g-C_3N_4/NiO composites highly depend on the amount of incorporated NiO. The photocatalytic activity of the CNN*x* samples gradually increases with the increase of the NiO loading amount from 0.01 to 0.03 g. The highest photocatalytic H_2 evolution rate of 170.60 μmol·g^{-1}·h^{-1} is reached in CNN3 sample, which is 8.3 times more than that of NV-g-C_3N_4. These results clearly demonstrate that more NiO loading amounts provide more active sites, and decrease the recombination of photoinduced e^-–h^+ in the photocatalytic H_2 production process. It is very similar to the reported phenomena in Refs. [25, 44, 47–49]. However, when the NiO loading amount further increases to 0.04 g, the photocatalytic activity of the CNN4 has a slight decrease. This can be ascribed to two facts: (i) when the content of NiO exceeds a certain value (0.03 g), there may be a light absorbing

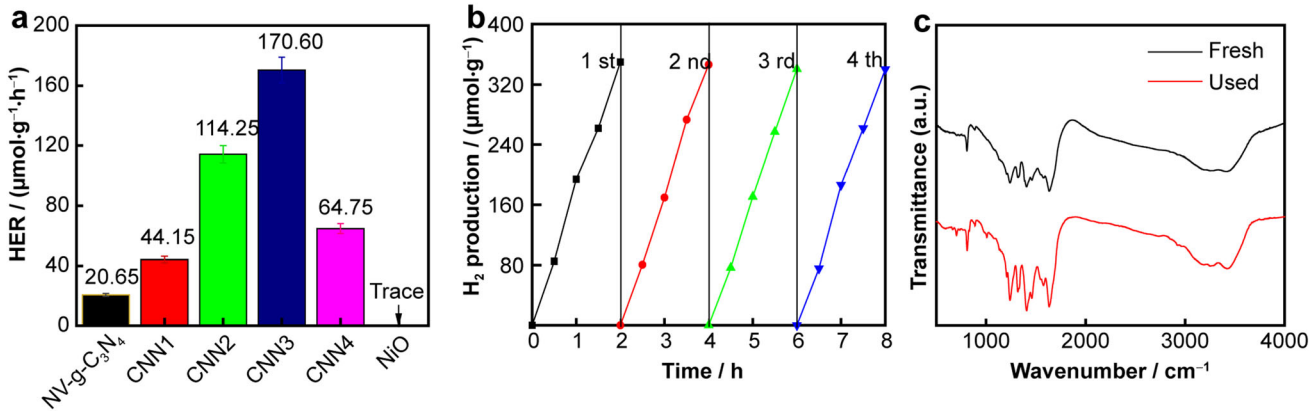

Fig. 8 **a** Rate constant (k) for photocatalytic H_2 evolution of all samples; **b** circulating runs of CNN3 under visible light irradiation and **c** FTIR patterns of CNN3 sample before and after 4-times circulating runs

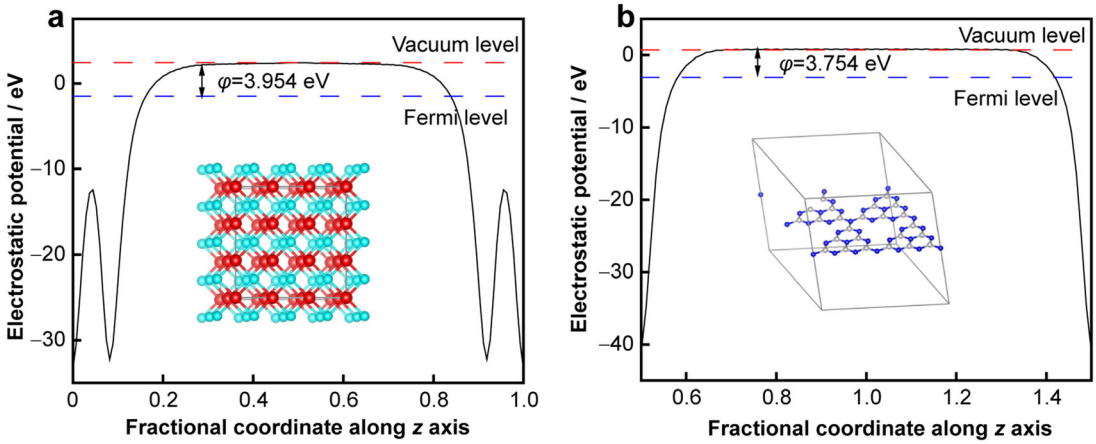

Fig. 9 E_F of **a** NiO (200) and **b** NV-g-C_3N_4, where insets show structural model of material for DFT calculation, and red and blue dashed lines denote vacuum level and Fermi level, respectively

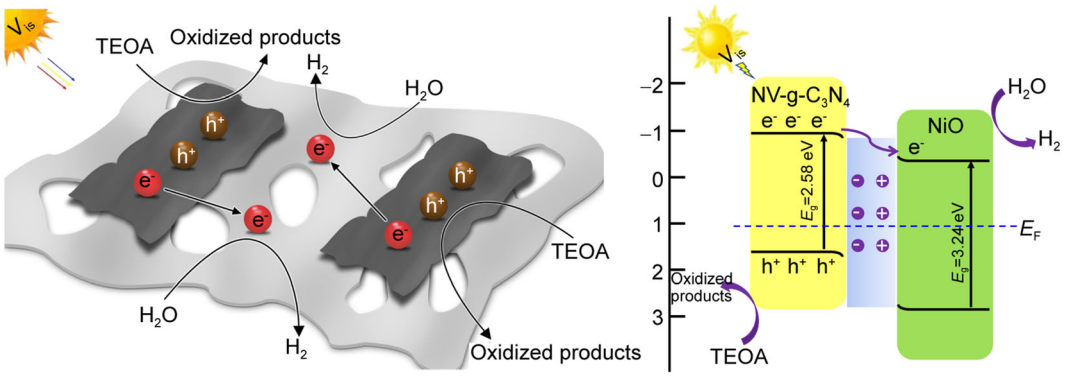

Fig. 10 Schematic diagram of photocatalytic mechanism for hybrid photocatalysts

competition between NV-g-C_3N_4 and NiO, which shields some visible light from arriving the surface of NV-g-C_3N_4, leading to a certain deactivation of photocatalytic H_2 evolution rate; (ii) the excessive NiO may perform as a kind of recombination center instead of providing an electron pathway [50].

Moreover, the stability of photocatalyst is another vital character to determine its sustainability [51, 52]. Here, as can be clearly seen from Fig. 8b, after four successive cycles, the H_2 evolution rate of CNN3 sample has no obvious decrease, implying high photo-stability of CNN3 sample [53]. Besides, FTIR spectra of CNN3 sample are almost the same before and after 4 cyclic tests, further verifying the sustainability of CNN3 [50, 54].

To understand the photocatalytic mechanism, the work function of NiO and NV-g-C_3N_4 simulated by DFT calculation is shown in Fig. 9. As shown, the NV-g-C_3N_4 has a smaller work function (3.754 eV) than NiO (3.954 eV). In general, the material work function is negatively related to its Fermi level. Accordingly, the NV-g-C_3N_4 possesses a higher Fermi level than NiO and thus the photogenerated electron in the NV-g-C_3N_4 CB will easily transfer to NiO under visible light irradiation [55].

Therefore, based on the above characterization and photocatalytic performance results, possible reaction mechanism for the CNN*x* samples through the addition of NiO as co-catalyst is proposed and shown in Fig. 10 [56]. The whole process is as follows: under visible light irradiation, NV-g-C_3N_4 is excited to provide the photo-generated electrons and holes, the electrons in the NV-g-C_3N_4 conduction band easily transfer to the NiO conduction band, and then reduce diffused water molecule to produce H_2 in the photocatalytic reaction. The residual holes in the NV-g-C_3N_4 valence band are consumed by the sacrificial agent triethanolamine in the system [57]. In this way, the photogenerated electron–hole pairs in the photocatalytic reaction are more easily separated, thus improving the activity of photocatalyst.

4 Conclusion

In summary, a non-noble metal hierarchical porous NiO modified NV-g-C_3N_4 photocatalyst is prepared. As expected, the CNN3 sample with an optimal mass ratio of NiO ($\sim$ 1.7%) has the highest H_2 evolution rate of 170.60 $\mu mol \cdot g^{-1} \cdot h^{-1}$, exhibiting $\sim$ 8.3-fold enhancement compared to that of NV-g-C_3N_4. Further research reveals that the hierarchical porous NiO as co-catalysts could provide more active sites for H_2 production. Moreover, the CNN*x* hybirds formed at interface between NiO and host nitrogen-vacated g-C_3N_4 create an interface electric field, which is in favor of the photogenerated electrons migration and separation from NV-g-C_3N_4 to NiO. Therefore, NiO modified NV-g-C_3N_4 photocatalysts show significantly enhanced visible light photocatalytic hydrogen production activity as compared to the singular NV-g-C_3N_4 and NiO sample. This work demonstrates that the hierarchical porous NiO can be applied as a cheap and efficient co-catalyst to replace expensive and rare noble metals in photocatalytic reactions, which might be extended to other functional materials.

Acknowledgements This study was financially supported by the National Natural Science Foundation of China (Nos. 22075072 and 52003079) and Hubei Provincial Natural Science Foundation of China (No. 2019CFB568).

References

[1] Chen GZ, Chen KJ, Fu JW, Liu M. Tracking dynamic evolution of catalytic active sites in photocatalytic CO_2 reduction by in situ time-resolved spectroscopy. Rare Met. 2020;39(6):607.

[2] Cheng TT, Sun XF, Xian T, Yi Z, Li RS, Wang XX, Yang H. Tert-butylamine/oleic acid-assisted morphology tailoring of hierarchical $Bi_4Ti_3O_{12}$ architectures and their application for photodegradation of simulated dye wastewater. Opt Mater. 2021;112:110781.

[3] Liu G, Wang GH, Hu ZH, Su YR, Zhao L. Ag_2O nanoparticles decorated TiO_2 nanofibers as a p-n heterojunction for enhanced photocatalytic decomposition of RhB under visible light irradiation. Appl Surf Sci. 2019;465:902.

[4] Zhao HY, Liu Q, Wang XX, Huo JR, Li L, Qian P, Su YJ. First-principles calculation of $Au_n@(ZnS)_{42}$ (n = 6–16) hetero-nanostructure system. Rare Met. 2020;39(10):1165.

[5] Lu LY, Wang GH, Xiong ZW, Hu ZF, Liao YW, Wang J, Li J. Enhanced photocatalytic activity under visible light by the synergistic effects of plasmonics and Ti^{3+}-doping at the Ag/TiO_{2-x} heterojunction. Ceram Int. 2020;46(8):10667.

[6] Mei ZH, Wang GH, Yan SD, Wang J. Rapid microwave-assisted synthesis of 2D/1D $ZnIn_2S_4/TiO_2$ S-scheme heterojunction for catalyzing photocatalytic hydrogen evolution. Acta Phys-Chim Sin. 2021;37(6):2009097.

[7] Wu XH, Gao DD, Wang P, Yu HG, Yu JG. NH_4Cl-induced low-temperature formation of nitrogen-rich g-C_3N_4 nanosheets with improved photocatalytic hydrogen evolution. Carbon. 2019;153:757.

[8] Pan ZM, Zhang GG, Wang XC. Polymeric carbon nitride/reduced graphene oxide/Fe_2O_3: all-solid-state Z-scheme system for photocatalytic overall water splitting. Angew Chem Int Ed. 2019;131(21):7102.

[9] Niu P, Liu G, Cheng HM. Nitrogen vacancy-promoted photocatalytic activity of graphitic carbon nitride. J Phys Chem C. 2012;116(20):11013.

[10] Hong ZH, Shen B, Chen YL, Lin BZ, Gao BF. Enhancement of photocatalytic H_2 evolution over nitrogen-deficient graphitic carbon nitride. J Mater Chem A. 2013;1(38):11754.

[11] Li XH, Zhang J, Zhou F, Zhang HL, Bai J, Wang YJ, Wang HY. Preparation of N-vacancy-doped g-C_3N_4 with outstanding photocatalytic H_2O_2 production ability by dielectric barrier discharge plasma treatment. Chin J Catal. 2018;39(6):1090.

[12] Wang K, Jiang LS, Wu XY, Zhang GK. Vacancy mediated Z-scheme charge transfer in a 2D/2D $La_2Ti_2O_7$/g-C_3N_4 nanojunction as a bifunctional photocatalyst for solar-to-energy conversion. J Mater Chem A. 2020;8(26):13241.

[13] Li JM, Zhao L, Wang SM, Li J, Wang GH, Wang J. In situ fabrication of 2D/3D g-C_3N_4/Ti_3C_2 (MXene) heterojunction for efficient visible-light photocatalytic hydrogen evolution. Appl Surf Sci. 2020;515(15):145922.

[14] Li J, Wang S, Sun G, Gao H, Yu X, Tang S, Zhao X, Yi Z, Wang Y, Wei Y. Facile preparation of $MgAl_2O_4/CeO_2/Mn_3O_4$ heterojunction photocatalyst and enhanced photocatalytic activity. Mater Today Chem. 2021;19:100390.

[15] Zhao GX, Sun YB, Zhou W, Wang XK, Chang K, Liu GG, Liu HM, Kako T, Ye JH. Superior photocatalytic H_2 production with cocatalytic Co/Ni species anchored on sulfde semiconductor. Adv Mater. 2017;29(40):1703258.

[16] Zhong W, Wu XH, Liu YP, Wang XF, Fan JJ, Yu HG. Simultaneous realization of sulfur-rich surface and amorphous nanocluster of NiS_{1+x} cocatalyst for efficient photocatalytic H_2 evolution. Appl Catal B. 2021;280:119455.

[17] Mao ZY, Chen JJ, Yang YF, Wang DJ, Bie LJ, Fahlman BD. Novel g-C_3N_4/CoO nanocomposites with significantly enhanced visible-light photocatalytic activity for H_2 evolution. ACS Appl Mater Interfaces. 2017;9(14):12427.

[18] Xu Y, Cao Q, Yi Z, Wu PH, Cai SS. Adjusting the energy bands of WO_3@ZnO nanocomposite heterojunction through the combination of WO_3 thin film to improve its photoelectric performance. IEEE Access. 2020;8:171350.

[19] Yosefi L, Haghighia M. Fabrication of nanostructured flowerlike p-BiOI/p-NiO heterostructure and its efficient photocatalytic performance in water treatment under visible-light irradiation. Appl Catal B. 2018;220:367.

[20] Zhu XB, Luo B, Butburee T, Zhu JW, Han S, Wang LZ. Hierarchical macro/mesoporous NiO as stable and fast-charging anode materials for lithium-ion batteries. Microporous Mesoporous Mater. 2017;238:78.

[21] Hu XC, Wang GH, Wang J, Hu ZF, Su YR. Step-scheme NiO/BiOI heterojunction photocatalyst for rhodamine photodegradation. Appl Surf Sci. 2020;511:145499.

[22] Liao YW, Wang GH, Wang J, Wang K, Yan SD, Su YR. Nitrogen vacancy induced in situ g-C_3N_4 homojunction for boosting visible light-driven hydrogen evolution. J Colloid Inter Sci. 2021;587:110.

[23] Wang P, Cao YJ, Xu SQ, Yu HG. Boosting the H_2-evolution performance of TiO_2/Au photocatalyst by the facile addition of thiourea molecules. Appl Surf Sci. 2020;532:147420.

[24] Cao YJ, Wang P, Fan JJ, Yu HG. Covalently functionalized graphene by thiourea for enhancing H_2-evolution performance of TiO_2 photocatalyst. Ceram Int. 2021;47(1):654.

[25] Gao DD, Liu WJ, Xu Y, Wang P, Fan JJ, Yu HG. Core-shell Ag@Ni cocatalyst on the TiO_2 photocatalyst: one-step

photoinduced deposition and its improved H_2-evolution activity. Appl Catal B. 2020;260:118190.
[26] Fu JW, Xu QL, Low JX, Jiang CJ, Yu JG. Ultrathin 2D/2D WO_3/g-C_3N_4 step-scheme H_2-production photocatalyst. Appl Catal B. 2019;243:556.
[27] Fu YJ, Liu CA, Zhu C, Wang HB, Dou YJ, Shi WL, Shao MW, Huang H, Liu Y, Kang ZH. High-performance NiO/g-C_3N_4 composites for visible-light-driven photocatalytic overall water splitting. Inorg Chem Front. 2018;5(7):1646.
[28] Wang M, Cheng JJ, Wang XF, Hong XK, Fan JJ, Yu HG. Sulfur-mediated photodeposition synthesis of NiS cocatalyst for boosting H_2-evolution performance of g-C_3N_4 photocatalyst. Chin J Catal. 2021;42(1):37.
[29] Gao HJ, Zhao XX, Zhang HM, Chen JF, Wang SF, Yang H. Construction of 2D/0D/2D face-to-face contact g-C_3N_4@Au@$Bi_4Ti_3O_{12}$ heterojunction photocatalysts for degradation of Rhodamine B. J Electron Mater. 2020;49:5248.
[30] Kong LQ, Ji YJ, Dang ZZ, Yan JQ, Li P, Li YY, Liu SZ. g-C_3N_4 loading black phosphorus quantum dot for efficient and stable photocatalytic H_2 generation under visible light. Adv Funct Mater. 2018;28(22):1800668.
[31] Yu HG, Ma HQ, Wu XH, Wang XF, Fan JJ, Yu JG. One-step realization of crystallization and cyano-group generation for g-C_3N_4 photocatalysts with improved H_2 production. Sol RRL. 2020;5(2):2000372.
[32] Wu XH, Ma HQ, Zhong W, Fan JJ, Yu HG. Porous crystalline g-C_3N_4: bifunctional $NaHCO_3$ template-mediated synthesis and improved photocatalytic H_2-evolution rate. Appl Catal B. 2020; 271:118899.
[33] Sun YL, Jin D, Sun Y, Meng X, Gao Y, Dall'Agnese YH, Chen G, Wang XF. g-C_3N_4/$Ti_3C_2T_x$ (MXenes) composite with oxidized surface groups for efficient photocatalytic hydrogen evolution. J Mater Chem A. 2018;6(19):9124.
[34] Chu JY, Han XJ, Yu Z, Du YC, Song B, Xu P. Highly efficient visible-light-driven photocatalytic hydrogen production on CdS/Cu_7S_4/g-C_3N_4 ternary heterostructures. ACS Appl Mater Interfaces. 2018;10(24):20404.
[35] Yang MQ, Dan JD, Pennycook SJ, Lu X, Zhu H, Xu QH, Fan HJ, Ho GW. Ultrathin nickel boron oxide nanosheets assembled vertically on graphene: a new hybrid 2D material for enhanced photo/electro-catalysis. Mater Horiz. 2017;4(5):885.
[36] Dong ZF, Wu Y, Thirugnanam N, Li GL. Double Z-scheme ZnO/ZnS/g-C_3N_4 ternary structure for efficient photocatalytic H_2 production. Appl Surf Sci. 2018;430:293.
[37] Tang JY, Guo RT, Zhou WG, Huang CY, Pan WG. Ball-flower like NiO/g-C_3N_4 heterojunction for efficient visible light photocatalytic CO_2 reduction. Appl Catal B. 2018;237:802.
[38] Elbanna O, Fujitsuka M, Majima T. g-C_3N_4/TiO_2 mesocrystals composite for H_2 evolution under visible-light irradiation and its charge carrier dynamics. ACS Appl Mater Interfaces. 2017; 9(40):34844.
[39] Han CQ, Zhang RM, Ye YH, Wang L, Ma ZY, Su FY, Xie HQ, Zhou Y, Wong PK, Ye LQ. Chainmail co-catalyst of NiO shell-encapsulated Ni for improving photocatalytic CO_2 reduction over g-C_3N_4. J Mater Chem A. 2019;7(16):9726.
[40] Liu MJ, Xia PF, Zhang LY, Cheng B, Yu JG. Enhanced photocatalytic H_2-production activity of g-C_3N_4 nanosheets via optimal photodeposition of Pt as cocatalyst. ACS Sustain Chem Eng. 2018;6(8):10472.
[41] Yuan YJ, Yang Y, Li ZJ, Chen DQ, Wu ST, Fang GL, Bai WF, Ding MY, Yang LX, Cao DP, Yu ZT, Zou ZG. Promoting charge separation in g-C_3N_4/graphene/MoS_2 photocatalysts by two-dimensional nanojunction for enhanced photocatalytic H_2 production. ACS Appl Energy Mater. 2018;1(4):1400.
[42] Wang J, Xia Y, Zhao HY, Wang GF, Xiang L, Xu JL, Komarneni S. Oxygen defects-mediated Z-scheme charge separation in g-C_3N_4/ZnO photocatalysts for enhanced visible-light degradation of 4-chlorophenol and hydrogen evolution. Appl Catal B. 2017;206:406.
[43] Yu HG, Xu JC, Gao DD, Fan JJ, Yu JG. Triethanolamine-mediated photodeposition formation of amorphous Ni-P alloy for improved H_2-evolution activity of g-C_3N_4. Sci China Mater. 2020;63(11):2215.
[44] Liu JN, Jia QH, Long JL, Wang XX, Gao ZW, Gu Q. Amorphous NiO as co-catalyst for enhanced visible-light-driven hydrogen generation over g-C_3N_4 photocatalyst. Appl Catal B. 2018;222:35.
[45] Shifa TA, Wang FM, Cheng ZZ, He P, Liu Y, Jiang C, Wang ZX, He J. High crystal quality 2D manganese phosphorus trichalcogenide nanosheets and their photocatalytic activity. Adv Funct Mater. 2018;28(18):1800548.
[46] Han YY, Lu XL, Tang SF, Yin XP, Wei ZW, Lu TB. Metal-free 2D/2D heterojunction of graphitic carbon nitride/graphdiyne for improving the hole mobility of graphitic carbon nitride. Adv Energy Mater. 2018;8(16):1702992.
[47] Ye LQ, Ma ZY, Deng Y, Ye YH, Wang L, Kou MP, Xie HQ, Xu ZK, Zhou Y, Xia DH, Wong PK. Robust and efficient photocatalytic hydrogen generation of ReS_2/CdS and mechanistic study by on-line mass spectrometry and in situ infrared spectroscopy. Appl Catal B. 2019;257:117897.
[48] Ran JR, Zhang J, Yu JG, Jaroniecc M, Qiao SZ. Earth-abundant cocatalysts for semiconductor based photocatalytic water splitting. Chem Soc Rev. 2014;43(22):7787.
[49] Yang JH, Wang DG, Han HX, Li C. Roles of cocatalysts in photocatalysis and photoelectrocatalysis. Acc Chem Res. 2013; 46(8):1900.
[50] Wang J, Wang GH, Jiang J, Wan Z, Su YR, Tang H. Insight into charge carrier separation and solar-light utilization: rGO decorated 3D ZnO hollow microspheres for enhanced photocatalytic hydrogen evolution. J Colloid Interface Sci. 2020;564:32.
[51] Kong LG, Dong YM, Jiang PP, Wang GL, Zhang HZ, Zhao N. Light-assisted rapid preparation of a Ni/g-C_3N_4 magnetic composite for robust photocatalytic H_2 evolution from water. J Mater Chem A. 2016;25(4):9998.
[52] Wang J, Wang GH, Wang X, Wu Y, Su YR, Tang H. 3D/2D direct Z-scheme heterojunctions of hierarchical TiO_2 microflowers/g-C_3N_4 nanosheets with enhanced charge carrier separation for photocatalytic H_2 evolution. Carbon. 2019;149: 618.
[53] Vu MH, Sakar M, Nguyen CC, Do TO. Chemically bonded Ni cocatalyst onto the S doped g-C_3N_4 nanosheets and their synergistic enhancement in H_2 production under sunlight irradiation. ACS Sustainable Chem Eng. 2018;6(3):4194.
[54] Obregón S, Colón G. Improved H_2 production of Pt-TiO_2/g-C_3N_4-MnO_x composites by an efficient handling of photogenerated charge pairs. Appl Catal B. 2014;144:775.
[55] Wang J, Wang GH, Cheng B, Yu JG, Fan JJ. Sulfur-doped g-C_3N_4/TiO_2 S-scheme heterojunction photocatalyst for Congo Red photodegradation. Chin J Catal. 2021;42(1):56.
[56] Yu HG, Yuan RR, Gao DD, Xu Y, Yu JG. Ethyl acetate-induced formation of amorphous MoS_x nanoclusters for improved H_2-evolution activity of TiO_2 photocatalyst. Chem Eng J. 2019; 375:121934.
[57] Shen RC, Xie J, Zhang HD, Zhang AP, Chen XB, Li X. Enhanced solar fuel H_2 generation over g-C_3N_4 nanosheet photocatalysts by the synergetic effect of noble metal-free Co_2P cocatalyst and the environmental phosphorylation strategy. ACS Sustain Chem Eng. 2018;6(1):816.